

Hindered Rotational Energy Barriers of BH_4^- Tetrahedra in $\beta\text{-Mg}(\text{BH}_4)_2$ from Quasielastic Neutron Scattering and DFT Calculations

D. Blanchard,^{*,†} J. B. Maronsson,^{†,‡} M. D. Riktor,[§] J. Kheres,[†] D. Sveinbjörnsson,[†] E. Gil Bardají,^{||} A. Léon,^{||} F. Juranyi,[†] J. Wuttke,[#] K. Lefmann,[†] B. C. Hauback,[§] M. Fichtner,^{||} and T. Vegge[†]

[†]Materials Research Division, Risø National Laboratory for Sustainable Energy, Technical University of Denmark, Building 228, P.O. Box 49, DK-4000 Roskilde, Denmark

[‡]Center for Atomic Scale Materials Design, Technical University of Denmark, DK-2800 Lyngby, Denmark

[§]Physics Department, Institute for Energy Technology, P.O. Box 40, NO-2027 Kjeller, Norway

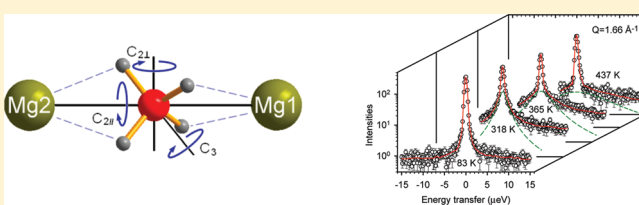
^{||}Institute of Nanotechnology, Karlsruhe Institute of Technology (KIT), P.O. Box 3640, D-76021 Karlsruhe, Germany

[#]Laboratory for Neutron Scattering, ETH Zurich and Paul Scherrer Institute, CH-5232 Villigen PSI, Switzerland

[¶]Forschungszentrum Jülich, JCNS at FRM II, Lichtenbergstrasse 1, 85747 Garching, Germany

[▽]Nanoscience Center, Niels Bohr Institute, Universitetsparken 5, bygn. D., Dk-2100 Copenhagen Ø. European Spallation Source, St. Algatan 4, 22100 Lund, Sweden

ABSTRACT: In this work, hindered rotations of the BH_4^- tetrahedra in $\text{Mg}(\text{BH}_4)_2$ were studied by quasielastic neutron scattering, using two instruments with different energy resolution, in combination with density functional theory (DFT) calculations. Two thermally activated reorientations of the BH_4^- units, around the 2-fold (C_2) and 3-fold (C_3) axes were observed at temperatures from 120 to 440 K. The experimentally obtained activation energies ($E_{\text{a}C_2} = 39$ and 76 meV and $E_{\text{a}C_3} = 214$ meV) and mean residence times between reorientational jumps are comparable with the energy barriers obtained from DFT calculations. A linear dependency of the energy barriers for rotations around the C_2 axis parallel to the Mg–Mg axis with the distance between these two axes was revealed by the DFT calculations. At the lowest temperature (120 K) only 15% of the BH_4^- units undergo rotational motion and from comparison with DFT results it is expectedly the BH_4^- units with the boron atom closest to the Mg–Mg axis, although dynamics related to local disorder existing at the boundary of the antiphase domains or to the presence of solvent in the sample cannot be strictly excluded. No long-range diffusion events were observed.



INTRODUCTION

Metal borohydrides are of interest as hydrogen storage materials due to their high volumetric and gravimetric capacity. However, as with many of the complex hydrides, they are hampered by slow absorption and desorption kinetics and poor reversibility.^{1–3}

Among the borohydrides, $\text{Mg}(\text{BH}_4)_2$ (Figure 1) and $\text{Ca}(\text{BH}_4)_2$ have more favorable thermodynamic stability than, for example, LiBH_4 , while maintaining attractive hydrogen storage capacities (14.9 and 11.5 mass %, respectively).^{2,4} Furthermore, for these two compounds, partial reversibility has been obtained by utilizing high pressure^{5–7} (60%–70% recovery of the borohydride) and in the case of $\text{Ca}(\text{BH}_4)_2$ at more moderate conditions by addition of catalysts (60% recovery⁸). Kinetic properties have also been shown to improve by using composite materials like $\text{Ca}(\text{BH}_4)_2 + \text{MgH}_2$.⁹

Borohydrides are largely ionic compounds with a general formula $\text{M}(\text{BH}_4)_n$, consisting of metal cations M^{n+} , the hydrogen atoms being covalently bound to the boron, forming tetrahedral BH_4^- . The possible hydrogen dynamics are long-range translational diffusion and localized motions such as rotations of the

BH_4^- complexes along specific axes, librations of the complexes, and vibrations within the complexes. Rotational dynamics are often coupled to order–disorder phase transition in coordination compounds,^{10,11} and the decomposition of borohydrides could possibly involve long-range diffusion of H and/or of the whole BH_4^- complex. The first results published on the rotational reorientation of the BH_4^- unit in borohydrides date back to the 1950s. At that time, researchers were interested in understanding the nature of the interactions influencing molecular reorientations in solids. To our knowledge, the first experimental study ever published, giving the energy barriers for the reorientations of BH_4^- in sodium, potassium, and rubidium borohydrides, was performed using nuclear magnetic resonance (NMR) and date from 1955,¹² while a second was published on lithium, sodium, and potassium borohydrides 14 years after,

Received: September 8, 2011

Revised: November 21, 2011

Published: November 22, 2011

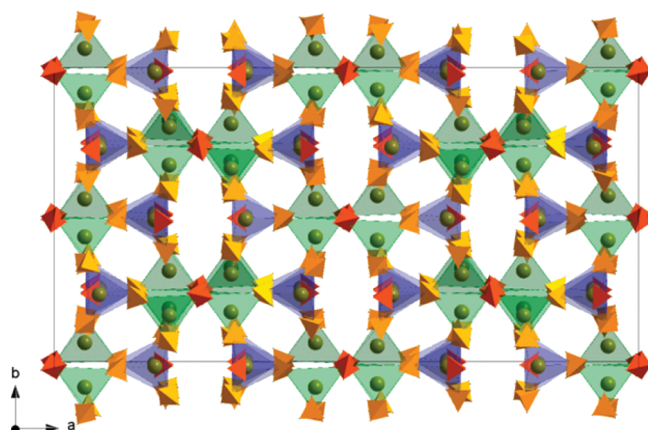


Figure 1. The idealized structure of $\beta\text{-Mg}(\text{BH}_4)_2$, space group $Fddd$,³³ viewed along the c axis: spheres, Mg atoms; $\text{Mg}_1\text{-B}$ tetrahedra, green; $\text{Mg}_2\text{-B}$ tetrahedra, blue; $\text{B}0i\text{-H}$ tetrahedra ($i = 1, 2, 4$), orange; $\text{B}0j\text{-H}$ tetrahedra ($j = 3, 5$) red (see Table 2).

in 1969.¹³ Then, using the theoretical developments made by King,¹⁴ the barrier heights in potential functions hindering the rotation of the borohydride group were obtained from measurement of the heat capacity of the solid phases.¹⁵ Later on, more NMR studies were published on different compounds: NaBH_4 ,^{16–18} LiBH_4 ,¹⁹ $\alpha\text{-Mg}(\text{BH}_4)_2$,²⁰ KBH_4 ,¹⁸ and $\text{La}(\text{BH}_4)_3$.²¹ It is only recently that quasielastic neutron scattering (QENS) measurements have been performed on borohydrides and the reorientation of the BH_4^- unit studied for NaBH_4 , LiBH_4 , KBH_4 , and $\beta\text{-Ca}(\text{BH}_4)_2$.^{22–28} Inelastic neutron scattering measurements have also been used to probe the librational^{29,30} and rotational²⁹ properties of some borohydrides. The measurements conducted on $\text{Ca}(\text{BH}_4)_2$ gave evidence for librational modes as the origin of phase transformations and emphasized the importance of the contribution of the vibrational entropy to the stability of the different polymorphs.³⁰

Noting, still, the lack of knowledge about the structural transition and decomposition mechanisms in borohydrides, we have investigated the hindered rotation of the BH_4^- units, using QENS, in magnesium borohydride. This method is optimal to study hydrogen dynamics due to the large incoherent scattering cross section of hydrogen compared to all other scattering signals.³¹

At least two different polymorphs of unsolvated $\text{Mg}(\text{BH}_4)_2$ have been observed experimentally: a low-temperature metastable α phase^{32,33} and a high-temperature β phase.³³ Other polymorphs were also observed using different procedure of synthesis³⁴ or high static pressure.³⁵ Furthermore, density functional theory calculations predict the existence of other stable or metastable structures.^{36–38} The α and β phases can be obtained separately or as a mixture depending on the synthesis conditions. The α phase, metastable below 453 K, will transform into the β phase and then decompose with hydrogen release through a multistep process.³⁹ The β phase is stable up to 613 K and when cooled to room temperature.⁴⁰ It is this polymorph that has been used for the quasielastic neutron scattering measurements.

The aim of the study was to investigate the hindered rotation of the BH_4^- tetrahedra. For that purpose, QENS measurement combined with density functional theory (DFT) calculations have been successfully applied, and the results are discussed in connection with the structural features of this borohydride.

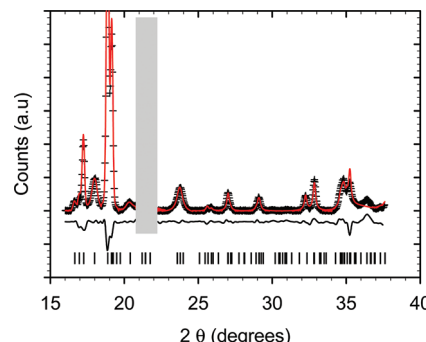
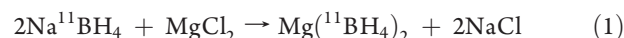


Figure 2. The XRD pattern of the as-prepared $\beta\text{-Mg}(\text{BH}_4)_2$. The dots are the experimental points, the line is the refined pattern based on the Rietveld method, and the bottom line is the difference between the experimental and the refined pattern. The ticks are the position of the Bragg peaks. The shadowed area corresponds to a broad peak due to the plastic film used to cover the sample. It is removed from the experimental data.

MATERIAL AND EXPERIMENTAL METHODS

Natural B contains 20% ^{10}B , which has a high absorption cross section. Therefore, to reduce neutron absorption, $\text{Mg}(\text{BH}_4)_2$ was synthesized via the metathesis reaction of eq 1 using a ^{11}B -enriched precursor (^{10}B cross section: 3837 barns versus 5.5×10^{-3} barns for ^{11}B).



A 2.50 g (0.066 mol) portion of $\text{Na}^{11}\text{BH}_4$ (purchased from Katchem Ltd., purity 99.8%) was first ball-milled for 4 h in a Fritsch P6 planetary mill at 600 rpm, with a ball to powder ratio of 25:1, and then added to 2.95 g (0.031 mol) of MgCl_2 (purchased from Sigma Aldrich, purity 98%) in 80 mL of diethyl ether (Et_2O). The mixture was heated under reflux at 40 °C overnight. After cooling down to room temperature, the suspension was filtered off and the filtrate was evaporated under vacuum to remove the solvent. The resulting $\text{Mg}^{(11)}\text{BH}_4_2 \cdot n\text{Et}_2\text{O}$ adduct was then dried under vacuum at 80 °C for 12 h. The white solid was manually ground in a mortar and subsequently dried under vacuum at 180 °C for 12 h to obtain $\beta\text{-Mg}(\text{BH}_4)_2$ as a single phase with an isolated yield (with respect to MgCl_2) of 1.25 g (74%).

A powder X-ray diffraction pattern (PXD) was recorded with a BRUKER D8 diffractometer (40 kV, 40 mA, Cu radiation $K\alpha = 1.542 \text{ \AA}$) (See Figure 2). The pattern consists of several broad and sharp peaks. The broad peaks correspond to the $(2n+1, 2n+1, 2n+1)$ reflections of the proposed $Fddd$ structure.³³ In that structure, the crystal, an almost purely ionic system,⁴¹ consists of corner-sharing tetrahedra with Mg^{2+} ions at the center and BH_4^- units at the vertices. Two boron atoms reside on the (16e, 16g) Wyckoff positions and the three others as well as the magnesium and hydrogen atoms occupy the (32h) Wyckoff general positions, resulting in five crystallographically inequivalent BH_4^- groups. Each of the two Mg tetrahedra is bonded to one tetrahedron with B at the 16e or 16g sites and three tetrahedra with B at the 32h sites. The B atoms are surrounded by two Mg atoms in a planar, almost linear configuration, and the Mg–B–Mg angles and Mg–B or Mg–Mg distances depend on the B sites (Table 1). The BH_4^- tetrahedra have bidentate orientations with two H atoms pointing toward Mg. To explain the broadening of the $(2n+1, 2n+1, 2n+1)$ reflections, Her et al.³³ suggested the existence of an antiphase boundary modification of

Table 1. β -Mg(BH_4)₂ Structural Parameters Obtained from Rietveld Refinement of PXD Pattern and DFT Calculations^a

space group <i>Fddd</i> (No. 70); <i>Z</i> = 64			
DFT	<i>a</i> = 37.231 00 Å	<i>b</i> = 18.93 Å	<i>c</i> = 10.937 Å
PXD	37.14(6)	18.65(6)	10.91(6)
ref 33	37.0720(10)	18.6476(6)	10.9123(3)
site	<i>x/a</i>	<i>y/b</i>	<i>z/c</i>
Mg1/32 h	0.0763 (0.077) ^b	0.2412 (0.250)	0.5349 (0.5381)
Mg2/32h	0.0538 (0.052)	0.9299 (0.929)	0.7565 (0.746)
B01/32h	0.4439 (0.444)	0.6372 (0.647)	0.5663 (0.560)
B02/32h	0.1074 (0.107)	1.0025 (1.008)	0.22306 (0.263)
B03/16e	0.3133 (0.312)	0 (0)	0 (0)
B04/32h	0.4444 (0.446)	0.1654 (0.153)	0.4046 (0.410)
B05/16g	0 (0)	0 (0)	0.7275 (0.773)
atom	Mg–Mg (Å) ^c	Mg–B–Mg (deg) ^c	<i>L</i> (Å) ^d
B01	4.77	161.87	0.68
B02	4.62	144.33	0.73
B03	4.71	156.86	0.47
B04	4.77	161.93	0.38
B05	4.80	172.52	0.16

^aIn both cases, the starting values were taken from ref 33. During Rietveld refinements, the atomic positions were not refined. ^bNumbers in brackets: parameters from ref 33. ^cAngles and distances calculated from the DFT relaxed structure. ^dDistance of the boron atom to the middle point of the Mg–Mg segment.

the *Fddd* super structure, coherent over long distances in the *bc* planes but with frequent defects in the *a* direction. These reflections were excluded for the Rietveld refinement performed with the Rietica software.⁴² The final fit was then obtained from the superposition of the Rietveld fit and individual fits of the (2*n* + 1, 2*n* + 1, 2*n* + 1) peaks with Voigt profiles (Figure 2). The atomic positions were kept fixed and only the cell parameters were refined. They are in good agreement with those found in ref 33 and those calculated by DFT for the *Fddd* structure (see Table 1). No other crystalline phases could be identified, but the presence of an unexplained broad peak (at 36.4°), together with some small mismatch in the peak intensities, is an indication of the presence of impurities in the compound.

Mass spectrometry measurements (MS), using an OmniStar (GSD 320) mass spectrometer, were performed on the gas released by the sample when heated under dynamical vacuum from room temperature up to 723 K (heating ramp of 1 K min⁻¹) (Figure 3). The signal for hydrogen showed several peaks in the temperature range 450–650 K, illustrating the multistep thermal decomposition process. The analysis of the measurement shows that H₂ accounts for ~96% of the released gas and Et₂O ~4%, the amount of H₂O, B₂H₆, and other gases like O₂ being negligible (<<1%). Thus, the amount of solvent left in the sample after its synthesis is rather low, but its contribution to the total H atomic content is not negligible. The sample appeared to be water-free.

QENS experiments were performed with two complementary instruments, SPHERES and MARS, in order to cover a wide energy range thanks to the two different energy resolutions. SPHERES⁴³ is a high-resolution neutron backscattering spectrometer located at FRM II (Forschungs-Neutronenquelle Heinz Maier-Leibnitz),

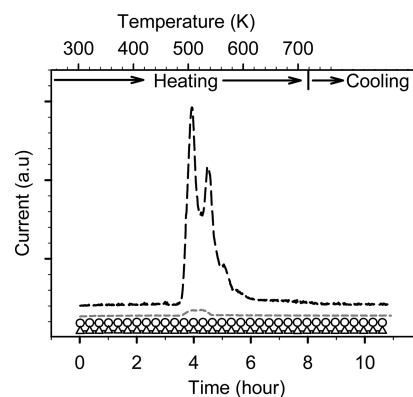


Figure 3. Mass spectrometry measurements. The sample was heated under dynamical vacuum from room temperature up to 723 K at a heating ramp of 1 K min⁻¹: (—) H₂ signal, (—) Et₂O signal, (-·-) B₂H₆ signal, and (-Δ-) H₂O signal.

Garching, Germany. MARS⁴⁴ is an inverted geometry time-of-flight spectrometer located at the Swiss Spallation Neutron Source (SINQ), Paul Scherrer Institute, Villigen, Switzerland.

The experiments at SPHERES were performed with ~0.08 g of Mg(¹¹BH₄)₂, which was loaded in an Al-wire-sealed, flat 30 × 40 × 0.5 mm³ Al container oriented at 135° with respect to the direct beam. Si(111) monochromator and analyzer crystals were used in a backscattering geometry, giving a final neutron wavelength of 6.271 Å and an energy resolution of 0.65 μeV with an energy transfer range selected of ±15.8 μeV. The spectra were recorded by nine detectors corresponding to a scattering vector ranging from 0.59 to 1.66 Å⁻¹. The data reduction was carried out with the SLAW package.⁴⁵

The experiments at MARS were performed with ~0.3 g of Mg(¹¹BH₄)₂, from the same batch, which was loaded in a double-walled Al container with height of 60 mm and inner and outer diameters of 9 and 10 mm, respectively. The spectra were recorded by five detectors on both sides of the instrument, corresponding to a scattering vector ranging from 0.49 to 1.86 Å⁻¹. Mica(006) analyzers were used in a backscattering geometry, giving a final neutron wavelength of 6.65 Å and an energy resolution of 13 μeV. The energy transfer window was chosen differently, depending on the width of the quasielastic signal, the largest being from -0.04 to 0.43 meV. The data reduction was carried out with the DAVE package.⁴⁶

■ DENSITY FUNCTIONAL THEORY CALCULATIONS

Theoretical calculations were used to identify the rate of possible dynamic events by calculating their energy barriers and prefactors. The calculations were performed using the Atomic Simulation Environment (ASE) package.⁴⁷ The DACAPO plane wave basis set implementation⁴⁸ was used to solve the electronic structure problem within the density functional theory (DFT) formalism.⁴⁹ The ion cores were described by ultrasoft pseudopotentials⁵⁰ and the exchange and correlation effects were described by the PW91 functional.⁵¹ The Kohn–Sham wave functions were expanded in a plane wave basis set with a cutoff energy of 350 and 600 eV for the density grid cutoff. The calculational cell contained 16 Mg(BH₄)₂ formula units, totaling 176 atoms in the β -phase structure,³³ no symmetry constraints were applied during its optimization. The wave functions were sampled using only the gamma point, which is well justified with

Table 2. Summary of the Experimental (QENS) Results for $\beta\text{-Mg}(\text{BH}_4)_2$

temp (K)	MARS	
	L_1	L_2
120	5×10^{-3}	—
150	11×10^{-2}	7.5×10^{-3}
180	18×10^{-2}	24×10^{-3}
210	25×10^{-2}	45×10^{-3}
240	32×10^{-2}	76×10^{-3}

temp (K)	SPHERES	
	L_1	
83	—	
318	1.94×10^{-3}	
365	5.11×10^{-3}	
437	16.2×10^{-3}	

such a large cell. Iterative relaxation using the limited memory Broyden–Fletcher–Goldfarb–Shanno algorithm⁵² was employed to obtain the ground state structure and unit cell parameter to a convergence of 0.001 eV/Å. The nudged elastic band (NEB) method,⁵³ along with the FIRE minimization algorithm,⁵⁴ was used to locate first-order saddle point configurations, to a convergence of 0.01 eV/Å, connecting two local minima. Within harmonic transition state theory (htST),⁵⁵ these configurations are used to determine the thermally activated reaction rates [$r(T)$], i.e., the barrier height (E_a) and the vibrational frequencies at the initial (ν_i^{IS}) and saddle points (ν_i^{TS}):

$$r(T) = \frac{\prod_{i=1}^{3N} \nu_i^{\text{IS}}}{\prod_{i=1}^{3N-1} \nu_i^{\text{TS}}} e^{-E_a/k_B T} \quad (2)$$

The vibrational frequencies were acquired using a finite difference approximation of the Hessian matrix (back and forward displacements of 0.01 Å). The term outside the exponential in eq 2, often referred as the prefactor, compares the vibrational frequencies at the initial state and saddle point. The characteristic times displayed in Table 3 are the reciprocal values of these prefactors.

RESULTS

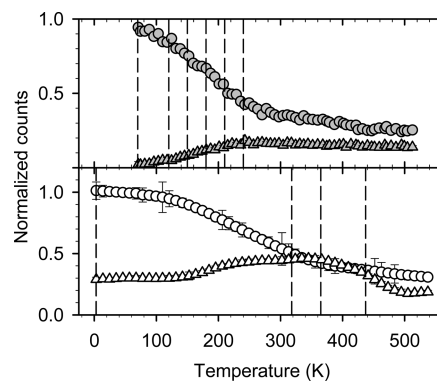
Quasielastic Neutron Scattering Spectra. Quasielastic temperature scans were performed with the two instruments. For each temperature, the spectra collected on each detector were summed to get one spectrum. The elastic intensities were obtained by adding up the counts with an energy transfer of $|\delta E| \leq 8 \mu\text{eV}$ (MARS) and $\leq 0.32 \mu\text{eV}$ (SPHERES). The quasielastic intensities were deduced by summing up the counts outside the elastic regions. Figure 4 displays the evolution with temperature of the normalized elastic ($I_{\text{N-el}}$) and quasielastic ($I_{\text{N-qel}}$) scattering measured at MARS and SPHERES.

At MARS, the sample was heated from 70 to 520 K and at 70 K no quasielastic broadening was detected since the hydrogen is “frozen in” on the time scale accessible with the instrument. On heating between 70 and 220 K, $I_{\text{N-el}} (|\delta E| \leq 8 \mu\text{eV})$ decreased

Table 3. Summary of the Experimental (QENS) and Computational (DFT) Results for $\beta\text{-Mg}(\text{BH}_4)_2$

	$\tau_0 (\times 100 \text{ ps})^a$		$E_a (\text{meV})^a$	
	C ₂	C ₃	C ₂	C ₃
MARS	61 ± 0.3	—	39 ± 0.5	—
	46 ± 0.15	—	76 ± 5	—
SPHERES	—	21 ± 0.3	—	214 ± 4
DFT	B01	15	1	82
	B02	26	5	96
	B03	17	3	60
	B04	14	6	54
	B05	25	4	28
				208

^a τ_0 and E_a experimental values were calculated from the Arrhenius fits [$\Gamma = \Gamma_0 \exp(-E_a/k_B T)$] of the experimental Lorentzian broadening and using eqs 6 and 7.

**Figure 4.** The normalized elastic and quasielastic intensities ($I_{\text{N-el}}$ and $I_{\text{N-qel}}$) during temperature scans: circles, $I_{\text{N-el}}$; triangles, $I_{\text{N-qel}}$; filled symbols, MARS intensities on heating from 70 to 520 K; open symbols, SPHERES intensities on heating from 3 to 540 K. The vertical lines are the temperatures at which the QENS spectra were measured.

while $I_{\text{N-qel}} (|\delta E| > 8 \mu\text{eV})$ slowly increased. The maximum $I_{\text{N-qel}}$ is at 220 K, followed by a plateau upon heating to the highest temperature. After the maximum, the hydrogen motion is too fast and the quasielastic broadening too large and thus partly falling outside the energy window chosen for MARS. The same intensity evolutions were observed when the sample was cooled back to 70 K, with a full recovery of the elastic intensity indicating no hydrogen desorption.

At SPHERES, the temperature scan from 10 to 540 K (Figure 4) was only performed during heating. In the temperature range from 10 to 120 K, the elastic intensity ($|\delta E| \leq 0.32 \mu\text{eV}$) decreased slowly while the quasielastic one ($|\delta E| > 0.32 \mu\text{eV}$) remained constant (measure of the background). At around 120 K, $I_{\text{N-el}}$ decreased faster while $I_{\text{N-qel}}$ started to increase with a maximum at 350 K and a decrease afterward. It then flattened out at around 500 K. At this temperature, the hydrogen motion gives rise to too large broadening for the instrument energy window. The temperatures to perform the detailed measurements were selected from these scans (see Table 2).

The QENS spectra were analyzed by using the curve fitting utility (PAN) included in the DAVE package. They consist of one elastic and some quasielastic components. The elastic component comes from the scattering process with no change in the

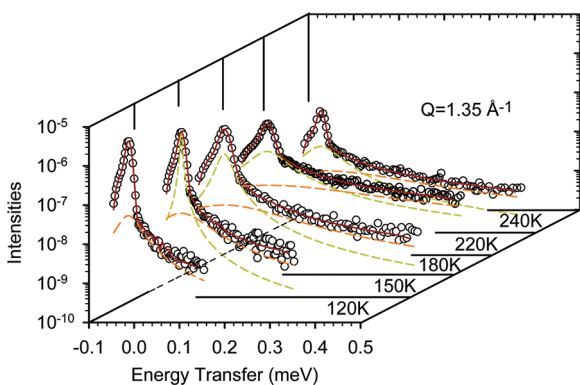


Figure 5. The QENS spectra of $\beta\text{-Mg}(\text{BH}_4)_2$ measured with MARS at different temperatures for $Q = 1.35 \text{ \AA}^{-1}$. The dots are the experimental data. The solid brown lines display the fits of the data, each consisting of a resolution broadened delta function, one or two Lorentzians (dashed light green and orange lines), and a flat background (not shown on the plots).

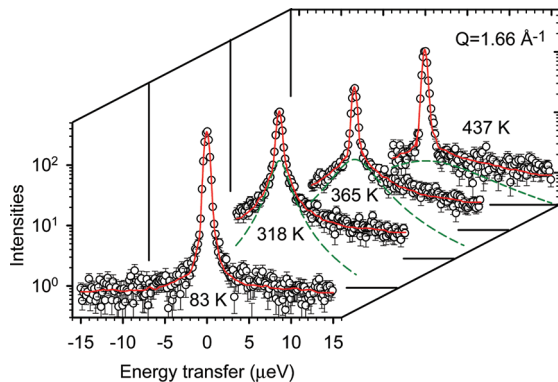


Figure 6. The QENS spectra of $\beta\text{-Mg}(\text{BH}_4)_2$ measured with SPHERES at different temperatures for $Q = 1.66 \text{ \AA}^{-1}$. The dots are the experimental data. The solid red lines display the fits of the data, each consisting of a resolution broadened delta function, a Lorentzian (dashed green lines), and a flat background (not shown on the plots).

neutron energy, while the quasielastic component reflects the energy transfer, gain and loss, due to the hydrogen motions. The measured total incoherent scattering function, $S_{\text{inc}}^{\text{tot}}(Q, \omega)$, is given by (see e.g. ref 31 for more details)

$$S_{\text{inc}}^{\text{tot}}(Q, \omega) = R(Q, \omega) \otimes \left(A_0(Q) \delta(\omega) + \sum_i A_i(Q) L(\Gamma_i, \omega) \right) + B(Q) \quad (3)$$

where $R(Q, \omega)$ is the instrumental resolution and $\delta(\omega)$ is the Dirac delta function describing the elastic scattering. $L(\Gamma_i, \omega)$ are Lorentzian functions that model the quasielastic signal with $\Gamma_i = \text{hwhm}$ (half-width at half-maximum). The B term represents the inelastic background in the quasielastic region. It can originate from processes that are much faster than those observable within the time scale of the instrument used. The term $A_0(Q)$ is the elastic incoherent structure factor (EISF)³¹ and its dependence on Q , the wave vector transfer, is important, since it basically determines the static properties of the number of sites accessible to the hydrogen atoms, the locations of these sites, and the normalized probability to be at a given site. It is a measurable

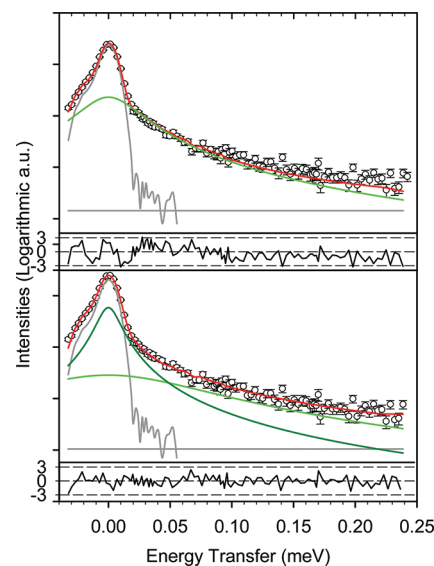


Figure 7. One QENS spectrum of $\beta\text{-Mg}(\text{BH}_4)_2$ measured with MARS at 180 K for $Q = 1.35 \text{ \AA}^{-1}$. The circles are the experimental data. The gray lines are the resolution function and the flat background, the green lines are the Lorentzian, and the red lines are the modeled spectra. The residuals of the fit are plotted below the spectra. The fit with one Lorentzian gives $\chi^2 = 2.8$ (upper plot), the fit with two Lorentzians (L_1 : light green, L_2 : dark green with $\Gamma_1 > \Gamma_2$) gives $\chi^2 = 1.7$ (lower plot).

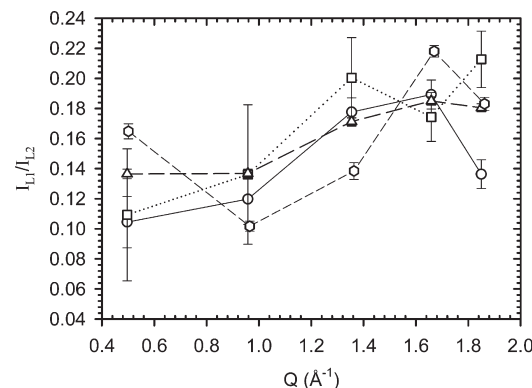


Figure 8. Ratio (I_{L_1}/I_{L_2} with $\Gamma_1 > \Gamma_2$) versus the wave vector transfer Q of the two Lorentzian intensities used to fit the spectrum measured with Mars at (○) 150 K, (□) 180 K, (Δ) 210 K, and (◇) 240 K.

quantity, evaluated from the ratio

$$A_0(Q) = \frac{I_{\text{el}}(Q)}{I_{\text{el}}(Q) + I_{\text{qel}}(Q)} \quad (4)$$

where $I_{\text{el}}(Q)$ and $I_{\text{qel}}(Q)$ are the integrated intensities of the elastic and quasielastic signal, respectively.

Herein and following eq 3, the QENS spectra were analyzed with the resolution-limited elastic peak, the delta function folded with the instrumental resolutions, and one or two Lorentzians, although the existence of five different crystallographic sites for the boron atoms should formally require the use of five Lorentzian. This approach was used since any attempt to fit the spectrum with more than two quasielastic components led to numerical instabilities or unrealistic results. The instrumental resolutions were obtained from measurements at 3 K (SPHERES) and 70 K (MARS).

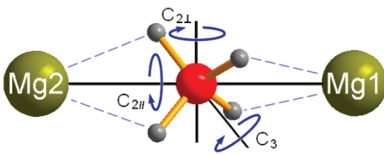


Figure 9. Schematic representation of the coordination environment, with the 2-fold $C_{2\parallel}$ - and $C_{2\perp}$ -axes and a 3-fold C_3 -axis, of a BH_4^- unit. From large to small size spheres: Mg, B, and H atoms. $C_{2\parallel}$ is the 2-fold axis in the direction of the Mg1–Mg2 axis, $C_{2\perp}$ is one of the axis perpendicular to the Mg1–Mg2 axis. The dashed lines represent the Mg–H bonds.

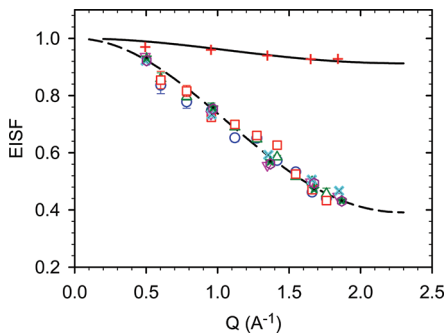


Figure 10. The measured and modeled EISFs: (---) $C_{2\parallel}$ (MARS data) and C_3 (SPHERES data) rotational diffusion model according to eq 5 and (—) according to eq 8. MARS: (red plus) 120 K, (blue x) 150 K, (red triangle) 180 K, (green asterisk) 210 K, and (black hexagon) 240 K. SPHERES: (red square) 318 K, (green triangle) 365 K, and (blue circle) 437 K.

At these temperatures no dynamical motion was observed on the time scale of the two instruments. The centers of the delta function and of the Lorentzian were constrained to be the same while their intensities were set free to adjust during the fitting procedure. For the measurements performed at MARS, since the energy window of the resolution function was smaller than those used for the measurements at higher temperatures, a flat fixed background was used. For the measurements performed with SPHERES, a flat background was used to model the too broad Lorentzian at high temperatures. Figures 5 and Figure 6 present typical examples of the spectra together with their fits with one or two Lorentzians. One Lorentzian was used to satisfactorily fit the spectra obtained with Mars at 120 K and SPHERES at 318, 365, and 437 K (typically with $\chi^2 < 2$). At higher temperatures, two Lorentzian (L_1 and L_2 with $\Gamma_1 > \Gamma_2$) were needed to fit the spectra obtained with Mars. Figure 7 displays a spectrum, for $Q = 1.35 \text{ \AA}^{-1}$, taken with MARS at 180 K. It emphasizes the need of two Lorentzians to obtain the best fit: with one Lorentzian, $\chi^2 = 2.8$ and with two, $\chi^2 = 1.7$. The analysis of the residual plots also confirms this latter point. In Figure 8 is plotted the ratio of the intensities of the two Lorentzians used to fit the spectra (I_{L_1}/I_{L_2} versus Q). For the four temperatures, the ratio can be considered as constant with only a slight increase with Q (from 0.14 to 0.18 on averages). A value of 0.16 ± 0.02 is obtained when averaging over all the values.

For all the temperatures, the widths of the Lorentzian functions were found to be Q -independent over the measured Q -range. This indicates that the observed quasielastic broadenings originated from localized hydrogen motion.³¹ The first obvious localized

motions are the rotations around the three 2-fold and four 3-fold axes of the BH_4^- units. To simplify the description, taking a linear configuration for the Mg–B–Mg, the 2-fold axis having the direction of the Mg–Mg axis will be noted $C_{2\parallel}$, while the two perpendicular ones will be noted $C_{2\perp}$ (see Figure 9).

For BH_4^- rotations around the C_2 -axes, the tetrahedral ions have two equal equilibrium orientations and the EISF is thus given by³¹

$$A_0(Q) = \frac{1}{2} \left(1 + j_0 \left(2 \frac{\sqrt{2}}{\sqrt{3}} Q d \right) \right) \quad (5)$$

where $j_0(x) = \sin(x)/x$ is the zeroth-order spherical Bessel function and d is the bond length between B and H. This rotation gives rise to one Lorentzian with a Q -independent hwhm of

$$\Gamma_{C_2} = 2\hbar\tau_2^{-1} \quad (6)$$

τ_2 is the average time between two successive reorientational jumps around the C_2 -axis, i.e., the average resident time of a hydrogen atom at a given site before jumping to a new site; thus its reciprocal value is the rotational frequency.

For BH_4^- rotations around the C_3 -axis, the tetrahedral ions have three equal equilibrium orientations and one hydrogen atom remains immobile. The expression for the EISF is identical to the rotation around the C_2 -axes (eq 5).³¹ It gives rise to one Lorentzian with a Q -independent hwhm of

$$\Gamma_{C_3} = \frac{3}{2}\hbar\tau_3^{-1} \quad (7)$$

τ_3 represents the average resident time for the reorientation around the 3-fold axes; its reciprocal value is the rotational frequency.

In the case where not all of the tetrahedra participate in the C_2 or C_3 rotations, i.e., only a fraction p of them undergoes the rotation, the EISF is expressed as

$$A_0(Q) = 1 - p + \frac{1}{2}p \left(1 + j_0 \left(2 \frac{\sqrt{2}}{\sqrt{3}} Q d \right) \right) \quad (8)$$

The experimental EISFs, extracted from the fitted QENS spectra (eq 4) provide strong evidence of the nature of the localized motion. Figure 10 displays the experimental and fitted EISFs. The model for the C_2 or C_3 hindered rotations (eq 5) follows the experimental data collected with MARS at 150, 180, 210, and 240 K and with SPHERES at 318, 365, and 437 K. The values for the best fits give $d = 1.22 \text{ \AA}$, which agrees with the average B–H distance obtained from DFT calculations. The model of eq 8 is used for the EISF of the measurement performed with MARS at 120 K, taking for granted that the dynamic events observed are also hindered rotation. In that case, only one Lorentzian was needed to fit the spectra. The B–H bond length, d , was kept constant ($d = 1.22 \text{ \AA}$) and the fitting parameter was p . A value of $p = 0.15$ is obtained; it is equivalent to say that, at this temperature, only 15% of the BH_4^- tetrahedra undergo hindered C_2 or C_3 rotation detectable with the MARS instrument, the other tetrahedra being seen as immobile.

Figure 11 displays the averaged, over all detectors, hwhm values versus the temperatures, together with the fits of the Arrhenius expression

$$\Gamma = \Gamma_0 \exp \left(\frac{-E_a}{k_B T} \right) \quad (9)$$

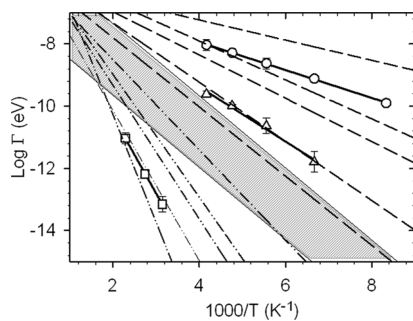


Figure 11. The thermally activated Arrhenius behavior of the hindered rotation of the BH_4^- units in $\beta\text{-Mg}(\text{BH}_4)_2$. The squares are the SPHERES experimental averaged hwhm values. The triangles and circles are the MARS experimental averaged hwhm's. The averaged hwhm's are fitted as $\Gamma = \Gamma_0 \exp(-E_a/k_B T)$ with (○) $\Gamma_0 = 2.14$ meV, $E_a = 39 \pm 0.5$ meV and (Δ) $\Gamma_0 = 2.86$ meV, $E_a = 76 \pm 5$ meV attributed to $C_{2\parallel}$ rotations and (□) $\Gamma_0 = 4.68$ meV, $E_a = 214 \pm 4$ meV attributed to C_3 rotations. The dashed lines are the theoretical values calculated for the five different crystallographic sites of the B atoms taking the energy barriers and prefactors obtained from DFT; (— · · —) hwhm's calculated for the C_3 rotations, (— · —) hwhm's calculated for the $C_{2\parallel}$ rotations. The shaded area represents the broadening that will give a process having typical resident times of 0.1–1 ps and $E_a = 100$ meV.

where the prefactor Γ_0 is a constant, E_a is the activation energy for the hindered rotation, k_B is the Boltzmann constant, and T the temperature. At 0 K, the activation energies equal the height of the potentials or energy barriers for hindered rotations, the contributions from the zero point energy (ZPE) being less than 20% of their magnitudes. To treat rates at final temperatures, where ZPE cannot just simply be added, the DFT calculated barrier heights are used and compared to the experimental activation energies.^{56,57} Straight lines for the thermally activated rotations were obtained with the following activation energies: MARS, 39 ± 0.5 and 76 ± 5 meV; SPHERES, 214 ± 4 meV (See Table 2 and Figure 11). Figure 11 also shows the hwhm values calculated using the DFT results (see the paragraph below).

DFT Calculations. The calculated structural parameters for the relaxed $\beta\text{-Mg}(\text{BH}_4)_2$ are displayed in Table 1. The atoms coordinates and cell parameters are in good agreement with those from ref 33 and the ones obtained from the Rietveld refinement of the diffraction pattern.

Her et al. performed the refinement of the structural parameters restricting the orientation of the two BH_4^- tetrahedron, with boron atoms at B03 (16g) and B05 (16e), to accommodate the $C_{2\parallel}$ -axis. During the DFT calculations, both the orientation of the tetrahedra and the positions of the boron were free to relax. While the orientations of the tetrahedra accommodate the $C_{2\parallel}$ -axis, all the boron atoms, including B03 and B05, move out of the Mg–Mg axis. The Mg–B–Mg angles, Mg–Mg distances, and the length (L) of the median of the Mg–B–Mg triangle, measuring the distance of the boron atom to the middle point of the Mg–Mg segment, can be found in Table 1. Figure 12 displays the experimental PXD pattern together with those simulated using the DFT calculated structure and those proposed by Her et al. At low angles, both patterns reproduce the experimental data. Only translation of the peak positions exist because of the different cell parameters, the ones obtained from DFT being slightly larger. Note that every $(2n+1, 2n+1, 2n+1)$ simulated reflection gives a sharp peak because the antiphase boundary is not modeled due to size limitations. At high angles, the discrepancy

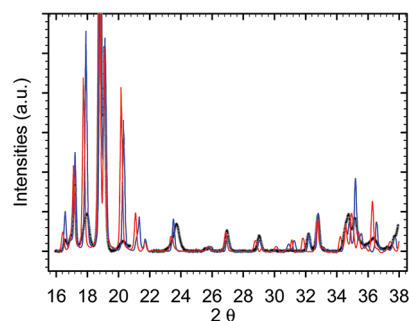


Figure 12. Gray line, experimental PXD pattern; red line, simulated X-ray pattern using the DFT relaxed structure; blue line, simulated X-ray pattern using the structure from ref 33.

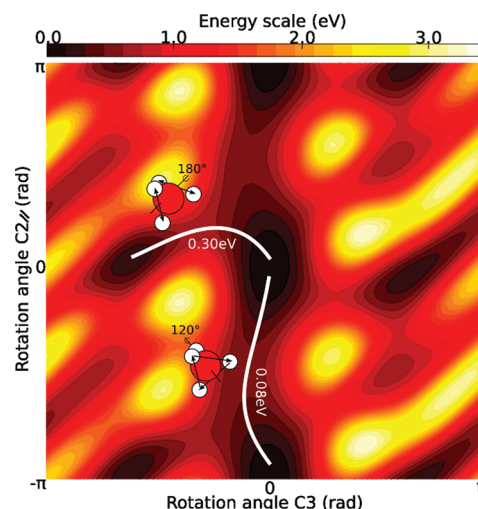


Figure 13. Potential energy surface for B01H_4^- rigid rotations along the $C_{2\parallel}$ - and C_3 -axes. The marked paths represent those chosen to do the NEB calculations. Their respective NEB barrier heights are written next to each one.

between the two simulated patterns is more pronounced and the one obtained from Her's structure is closer to the experimental one. The discrepancy, at high angles, between the DFT calculated pattern with the other ones might be due to the overestimated local disorder of the calculated structure.

The results from the QENS experiments showed localized dynamic events expected to originate from hindered rotations of borohydride units. Using the Schönflies notation⁵⁸ there are four different types of permutations possible for a single tetrahedral borohydride group. S_4 axes and mirror planes can be quickly discarded, as they are not rotations but rearrangements of hydrogen atoms that are much higher in energy, due to the required formation of planar BH_4^- configuration during the rearrangement. Then only various C_2 - and C_3 -axes remain. Since the boron positions are not equivalent, investigations of the hindered rotations using the NEB method had to be conducted for the five different positions, the three C_2 - and four C_3 -axes. Rapidly, the hindered rotations around the $C_{2\perp}$ -axes were discarded as leading to combinations with rotation around the C_3 -axes. For the rotation around the C_3 -axes, only a single axis of rotation per boron atom was retained, the others giving too high energy compared with those obtained experimentally.

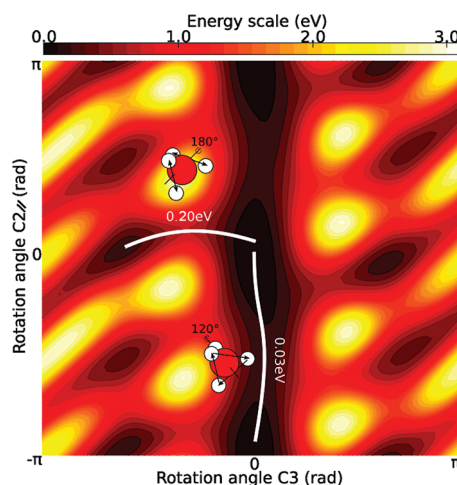


Figure 14. Potential energy surface for $\text{B}05\text{H}_4^-$ rigid rotations along the $C_{2\parallel}$ - and C_3 -axes. The marked paths represent those chosen to do the NEB calculations. Their respective NEB barrier heights are written next to each one.

Figures 13 and 14 present 2D rigid rotation potential energy surfaces (PES) for two of the symmetry-inequivalent BH_4^- units, B01 and B05, respectively, calculated using the $C_{2\parallel}$ -axis and a C_3 -axis as the degrees of freedom. The starting point for the calculation is the relaxed structure, and thus, the origin of the axis represents an energy minimum. As expected from their symmetry, energy minima for the rotations around the $C_{2\parallel}$ -axis occur at π and around the C_3 -axis at $2\pi/3$ and $4\pi/3$. Furthermore, some intermediate minima were found, but further calculations showed that they were very shallow once fully relaxed with energy barriers of low values compared to those obtained experimentally. It can be seen from these figures that the rotations around the $C_{2\parallel}$ -axis require lower energy than the one around the C_3 -axis, and this was true for all the inequivalent boron sites. The barrier heights calculated from the rigid rotation being higher than the barriers suggested by the experiments, NEB calculations were carried out with all the atoms in the supercell free to move. Figure 15 displays, as an example, the energy profile of these calculations for the B05 atom. A very shallow intermediate state (4×10^{-3} eV) is located at the top of the $C_{2\parallel}$ rotation. NEB calculations yielded barriers and quasielastic broadenings in good quantitative agreement with those of the experiments. The different energy barriers and prefactors can be found in Table 3. Figure 11 displays, together with the experimental values, the values of the hwhm calculated for the five different crystallographic sites of the B atoms using the energy barriers and prefactors obtained from the DFT calculations and eq 9. Figure 16 shows the QENS spectra measured with SPHERES, for $Q = 1.42 \text{ \AA}^{-1}$, together with the calculated spectra consisting of the sum of the resolution function and five Lorentzian of widths calculated using the energy barriers and prefactors obtained from the DFT calculation and eq 9. On this figure, the relative intensities of the Lorentzian and resolution function were set to comply with the EISF for the C_3 rotation (eq 5). At $Q = 1.42 \text{ \AA}^{-1}$, $\text{EISF} = 0.5$ thus $I_{\text{el}} = I_{\text{qel}}$ with $I_{\text{qel}} = 1/5\sum_i I_{L_i}$. Without any kind of adjustment or fitted parameters, the experimental data are fairly well described; nevertheless, the values for χ^2 ranging from 4.78 to 9.75 are larger than the one obtained when performing the fits with one or two Lorentzian plus background ($\chi^2 < 2$).

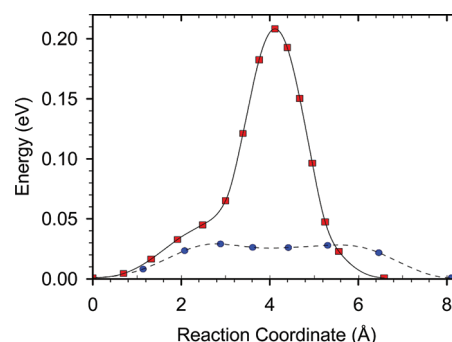


Figure 15. The calculated minimum energy path for the $C_{2\parallel}$ (blue/circles) and C_3 (red/squares) rotations of $\text{B}05\text{H}_4^-$. Each point is an NEB image; the lines are interpolations between them using also the forces. The reaction coordinate is the additive motion of atoms in the supercell.

A linear relationship exists between the energy barriers calculated for the hindered rotation around the $C_{2\parallel}$ -axis and the distance L of the boron atoms to the middle point of the Mg–Mg segments (See Figure 15). The simple correlation of L with the C_3 barriers does not hold, so other criteria have to be taken into account.

■ DISCUSSION

$\beta\text{-Mg}^{(11)\text{BH}_4}_2$ presents a structure with five different crystallographically distinct BH_4^- anions, so one should expect a distribution of the activation energies and rotational barriers and thus a distribution of the rotational frequencies and quasielastic broadenings. Herein the analysis of the QENS spectra was performed with a maximum of two Lorentzians for two main reasons. First, any attempt to fit the QENS spectrum with five Lorentzians, even with their relative intensities or hwhm's fixed, led to unrealistic results. Second, the quality of the outcomes, with a limited number of Lorentzians, is satisfactory not to use other models. Indeed if particular temperature dependence of the width of the quasielastic component, due to their distribution, were found, one should have considered using the formalism developed by Chahid et al.⁵⁹ for example. The method used herein leads to the overestimation of the low-frequency reorientational events with the one Lorentzian (SPHERES) or the sharper one (MARS) reproducing the main feature of the QENS spectra, i.e., the quasielastic broadening close to the resolution function while the high-frequency events are taken into account by the flat background. For that reason, the experimental values obtained for the reorientational frequencies have to be considered as semiquantitative, while the values for the activation energies should represent average values for the distribution.

The analysis of the QENS data obtained for $\beta\text{-Mg}^{(11)\text{BH}_4}_2$ has shown that, within the time scale accessible by the two instruments used, two different types of thermally activated hindered rotations of the BH_4^- unit were observed in the temperature range from 120 to 437 K. From the comparison of the experimental results to the DFT calculations, it is established that these rotations occur around the $C_{2\parallel}$ - and C_3 -axes. The experimental activation energy and the DFT calculated energy barriers are in good agreement with $E_{\text{a}C_{2\parallel}} = 39 \pm 0.5$ and 76 ± 5 meV determined experimentally to be compared with DFT values ranging from 28 to 82 meV and $E_{\text{a}C_3} = 214 \pm 4$ meV with DFT values ranging from 177 to 298 meV. The calculated prefactors

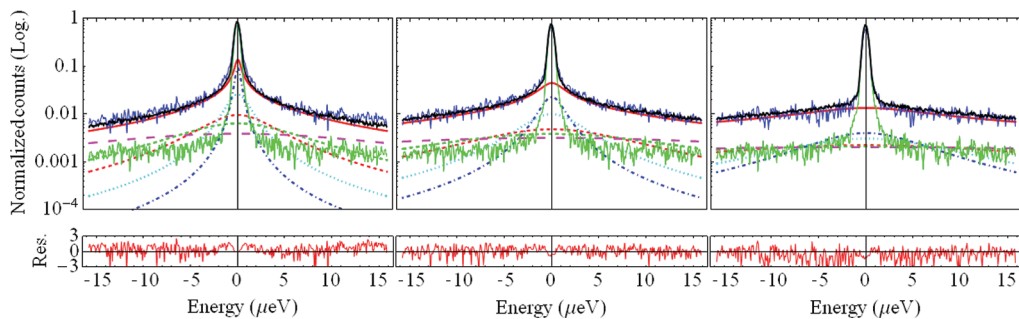


Figure 16. The QENS spectra of $\beta\text{-Mg}(\text{BH}_4)_2$ measured with SPHERES at different temperatures (from left to right, 318, 365, 437 K) for $Q = 1.42 \text{ \AA}^{-1}$. The blue lines are the experimental data. The black lines are the calculated spectra consisting of the sum of the resolution function (green lines) and five Lorentzian (dashed lines). The red lines represent the sum of the five Lorentzian. The widths of the Lorentzian are calculated using the DFT calculated energy barriers and prefactors and eq 9. The relative intensities of the Lorentzian and resolution function are set to comply with the EISF for the C_3 rotations (eq 5): $I_{\text{resolution}}(Q)/[I_{\text{resolution}}(Q) + 1/5\sum_1^5 I_{\text{resolution}}(Q)] = 1/2[1 + j_0[2(\sqrt{2}/\sqrt{3})Qd]]$. From left to right, $\chi^2 = 4.78, 3.22, 9.75$, respectively.

are somewhat smaller than the experimental values but still within the accuracy of the calculations and experiment. Together with the calculated energy barriers, good quantitative agreement with the experimental rotational frequencies at any given temperatures is obtained (see Table 3 and Figure 11). DFT calculation shows that even if all the Mg–B–Mg units are close to linear and the BH_4^- have bidentate orientations corresponding to the $C_{2\parallel}$ -axis, small variations of the distance L (length of the median of the Mg–B–Mg triangle) lead to noticeable differences in the energy barriers. With MARS, two distinct values were obtained. At the lowest temperature, the observed hydrogen dynamic, treated as hindered rotation, gave that $\sim 15\%$ of the hydrogen atoms are moving. This dynamic was also observed at higher temperatures, and when two Lorentzians were used, their relative intensities remained constant for all Q and temperatures with a ratio of $I_{L_1}/I_{L_2} = 0.16 \pm 0.02$. An activation energy of 39 meV was found for this dynamic. When compared to the DFT results it could correspond to the rotation around the $C_{2\parallel}$ -axis of the tetrahedron with B05 as centers which account for 12.5% of the BH_4^- (calculated energy barrier: 28 meV) and would give $I_{L_1}/I_{L_2} = 0.143$. This result is further supported by the agreement between the theoretical and experimental EISF, the latter being calculated by adding up the two contributions from the two Lorentzians for the evaluation of I_{qel} . Nevertheless and despite these proofs other arguments could be found to contradict this analysis. Second, local disorders and amorphous regions might exist at the antiphase boundary domains and it cannot be discarded that the low energy barrier events observed take place at these boundaries. Finally, the presence of Et_2O in the sample has to be considered with the reorientations of the methyl and ethyl group and other vibrational modes. The activation energies for the reorientations of the methyl or ethyl group are found to be around 100 meV.⁶⁰ Taking as prefactor typical Debye–Waller frequencies of 10^{12} – 10^{13} Hz leads to the shadowed area drawn in Figure 11, with no overlap with the measured quasielastic broadenings. Thus, it is unlikely that the reorientation associated with Et_2O appeared in the measured QENS data; however, this cannot be strictly rejected, and measurement with a solvent-free sample should be performed to definitively answer the question.

More generally, the rotations about the $C_{2\parallel}$ -axis were found to be energetically more favorable than those around the C_3 -axis. This can be easily explained, as suggested in ref 20, by looking at the schematic representation of the local environment of the BH_4^- tetrahedra (Figure 9). With the bidentate orientation,

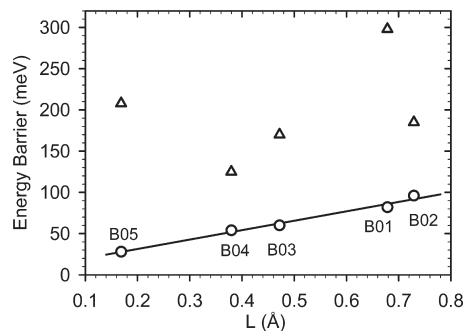


Figure 17. DFT calculated energy barriers for the hindered rotations versus L (length of the median of the Mg–B–Mg triangle): (Δ) energy barriers for the rotations around a C_3 -axis and (\circ) energy barriers for the rotations around a $C_{2\parallel}$ -axis.

no Mg–H bond is broken during rotation around the $C_{2\parallel}$ -axis, while the rotations around the C_3 -axis induce two bonds breaking and the one around the $C_{2\perp}$ -axis, four bond breakings.

In ref 20, the authors performed NMR measurements of the ^1H and ^{11}B spin–lattice relaxation rates in the low-temperature α phase of $\text{Mg}(\text{BH}_4)_2$ over the temperature range from 82 to 443 K. They observed three hydrogen dynamics with different activation energies and attributed them to reorientational motion of the BH_4^- unit. The averaged activation energies associated with those three processes were 116 ± 6 , 192 ± 12 , and 362 ± 5 meV, for the fastest to the slowest process, respectively, the fastest one “being characterized by a certain distribution of activation energy”. $\alpha\text{-Mg}(\text{BH}_4)_2$ crystallizes in the $P6_{1}22$ space group.⁶¹ It has six inequivalent crystallographic BH_4^- groups, each surrounded by two Mg atoms in a nearly linear configuration similar to the one existing in $\beta\text{-Mg}(\text{BH}_4)_2$. The authors suggested that the three observed processes originate from rotations around the $C_{2\parallel}$ -axis, inducing no bond breaking, the C_3 -axis, with two bond breaking, and the $C_{2\perp}$ -axis, with four bond breaking, the magnitude of the activation energies being correlated with the number of broken bonds.

The Mg–B and Mg–Mg distances are almost identical for the α and β structures (Mg–B $\sim 2.4 \text{ \AA}$ and Mg–Mg $\sim 4.8 \text{ \AA}$), but the distance L is smaller for the α structure (from 0.025 to 0.16 \AA) and the Mg–B–Mg angles vary from $\sim 147^\circ$ to 170° . From the linear dependency of $E_{\text{a}C_{2\parallel}}$ with L , obtained from the DFT results for the β structure (Figure 17), and with the value of $\bar{L} = 6.15 \times 10^{-2} \text{ \AA}$, we obtain $E_{\text{a}C_{2\parallel}} = 15.6 \text{ meV}$, which is an order of

magnitude smaller than the value 116 ± 6 meV attributed to this motion in ref 20. NMR and QENS results are consistent; see for example refs 19 and 25. Then two possible explanations exist, one being that the linear relationship found for the β phase does not hold in the case of the α structure and the other being that the observed dynamics were wrongly attributed.

In order to better understand the borohydrides and more generally complex hydrides used as hydrogen storage media, more knowledge has to be gathered about their decomposition mechanisms with atomic level information on the hydrogen dynamics. In LiBH_4 , motion of entire BH_4^- units has been identified as the main mass transport mechanism above the melting temperature,^{62,63} while at low temperatures a net transport of atomic hydrogen, probed by hydrogen/deuterium exchange, was also observed, although at a very low rate.^{64,65} Together with hindered rotation, long-range diffusion was observed for $\text{Ca}(\text{BH}_4)_2$,²⁷ but this was most probably due to the presence of trapped H_2O or H_2 in the compound. The hydrogen dynamics in NaAlH_4 and Na_3AlH_6 were also studied using quasielastic neutron scattering. One study showed only limited hydrogen vacancy diffusion, not influenced by the use of Ti additive,²³ while in another one quasielastic signal could be attributed to internal rotations and the possible combination of jumps with similar frequencies but different jump lengths.⁶⁶ This later study furthermore opens up new perspectives for time-resolved neutron backscattering studies and investigations of reaction kinetics. In other works,^{25,24,26} the rotational reorientation of the BH_4^- unit in MBH_4 ($\text{M} = \text{Na}, \text{Li}$, and K) was observed but no long-range diffusion. From the results presented in this study, no long-range hydrogen dynamics have been detected and only hindered rotations of the BH_4^- tetrahedra were observed. Part of the measurements, not shown herein, consisted of exposing for long period of time the samples to temperatures close to the decomposition temperature (500 K), aiming at monitoring any possible long-range diffusion of hydrogen at temperatures close to the thermal decomposition of the borohydride. During this measurement, the elastic intensity decreased, a sign that more and more hydrogen moved and probably left the sample, while the quasielastic intensity remained constant basically as a flat background. Thus, if any hydrogen diffusion events occurred, they were either too fast or too slow to be probed with the instruments used herein. For further investigations of diffusion events, one should consider using spin-echo or direct geometry time-of-flight spectrometers, allowing the observations of slower and faster motions respectively and the use of different neutron energies.

The combined DFT-QENS approach has been shown to be very useful both in the interpretation of the data and to determine crucial quantities useful to develop new experiments, including the characteristic times and the energies barriers.

In the time between the acceptance for the publication of this manuscript and its proof reading, a study on in-situ neutron diffraction of the deuteration of isotopic Mg^{11}B_2 has been published.⁶⁷ In this study, the $Fddd$ structure is retained but with slightly different positions for the D atoms when compared to the positions of the H atoms in ref 33. Furthermore, the $(2n+1, 2n+2, 2n+1)$ broad reflections are attributed to microstructural features rather than anti-phase boundaries, and quantitative phase analysis of the isotopic sample indicated that ca. 10% of B atoms are in a non-crystalline state with the possible existence of amorphous $\text{Mg}(\text{BD}_4)_2$.

AUTHOR INFORMATION

Corresponding Author

*E-mail: dibl@risoe.dtu.dk.

ACKNOWLEDGMENT

This work is based on experiments performed at the Swiss spallation neutron source SINQ, Paul Scherrer Institute, Villigen, Switzerland, and at FRMII, JCNS Garching, Germany. It has been supported by the Danish Council for independent Research through DANSCATT. The authors acknowledge the European Graduate School for Sustainable Energy Technology and the Nordic Center for Excellence on Hydrogen Storage Materials. The Danish Center for Scientific Computing is acknowledged for supercomputer access. The Center for Atomic Materials Design (CAMD) is supported by the Lundbeck Fondation. Financial support by EU-IP NESSHY (contract #518271) and the ERA-NET project "Hy-CO" is also gratefully acknowledged.

REFERENCES

- (1) Züttel, A.; Rentsch, S.; Fischer, P.; Wenger, P.; Sudan, P.; Mauron, P.; Emmenegger, C. *J. Alloys Compd.* **2003**, *356–357*, 515.
- (2) Nakamori, Y.; Miwa, K.; Ninomiya, A.; Li, H.; Ohba, N.; Towata, S.-I.; Züttel, A.; Orimo, S.-I. *Phys. Rev. B* **2006**, *74*, 045126–04519.
- (3) Hummelshøj, J. S.; et al. *J. Chem. Phys.* **2009**, *131*, 014101.
- (4) Miwa, K.; Aoki, M.; Noritake, T.; Ohba, N.; Nakamori, Y.; Towata, S.-I.; Züttel, A.; Orimo, S.-I. *Phys. Rev. B* **2006**, *74*, 155122–1551–5.
- (5) Chong, M.; Karkamkar, A.; Autrey, T.; Orimo, S.-I.; Jalasatgi, S.; Jensen, C. M. *Chem. Commun.* **2011**, *47*, 1330.
- (6) Severa, G.; Rönnebro, E.; Jensen, C. M. *Chem. Commun.* **2010**, *46*, 421.
- (7) Rönnebro, E.; Majzoub, E. H. *J. Phys. Chem. B* **2007**, *111* (No. 42), 12045.
- (8) Kim, J.-H.; Shim, J.-H.; Cho, Y. W. *J. Power Sources* **2008**, *181* (1), 140.
- (9) Barkhordarian, G.; Jensen, T. R.; Doppiu, S.; Rösenberg, U.; Borgschulte, A.; Gremaud, R.; Cerenius, Y.; Dornheim, M.; Klassen, T.; Bormann, R. *J. Phys. Chem. C* **2008**, *112*, 2743.
- (10) Lodzianna, Z.; Vegge, T. *Phys. Rev. Lett.* **2006**, *97* (11), 119602.
- (11) Tekin, A.; Hummelshøj, J. S.; Jacobsen, H. J.; Sveinbjörnsson, D.; Blanchard, D.; Nørskov, J. K.; Vegge, T. *Energy Environ. Sci.* **2010**, *3*, 448.
- (12) Ford, P. T.; Richards, R. *Discuss. Faraday Soc.* **1955**, No. 19, 230.
- (13) Tsang, T.; Farrar, T. C. *J. Chem. Phys.* **1969**, *50* (8), 3498.
- (14) King, H. F.; Hornig, D. F. *J. Chem. Phys.* **1966**, *44*, 4520.
- (15) Smith, D. *J. Chem. Phys.* **1974**, *60* (3), 958.
- (16) Trokiner, A.; Theveneau, H.; Papon, P. *J. Chem. Phys.* **1977**, *69* (2), 742.
- (17) Tarasov, V. P.; Bakum, S. I.; Privalov, V. I.; Shamov, A. A. *Russ. J. Inorg. Chem.* **1990**, *35*, 2096.
- (18) Babanova, O. A.; Soloninin, A. V.; Stepanov, A. P.; Skripov, A. V.; Filinchuk, Y. *J. Phys. Chem. C* **2010**, *114*, 3712.
- (19) Skripov, A. V.; Soloninin, A. V.; Filinchuk, Y.; Chernyshov, D. *J. Phys. Chem. C* **2008**, *112*, 18701.
- (20) Skripov, A. V.; Soloninin, A. V.; Babanova, O. A.; Hagemann, H.; Filinchuk, A. *J. Phys. Chem. C* **2010**, *114*, 12370.
- (21) Volkov, V.; Khikmatov, M.; Mirsaidov, U.; Gabuda, S.; Kozlova, S. G. *J. Struc. Chem.* **1988**, *29* (1), 58.
- (22) Butcher, F.; Lodzianna, Z.; Remhof, A.; Friederichs, O.; Borgschulte, A.; Mauron, P.; Züttel, A.; Sheptyakov, D.; Barkhordarian, G.; Bormann, R.; Chlopek, K.; Fichtner, M.; Sørby, M.; Riktor, M.; Hauback, B.; Orimo, S. *J. Phys. Chem. B* **2008**, *112*, 8042.

- (23) Shi, Q.; Voss, J.; Jacobsen, H. S.; Lefmann, K.; Zampomi, M.; Vegge, T. *J. Alloys Compd.* **2007**, *446–447*, 469.
- (24) Remhof, A.; Łodziana, Z.; Butcher, F.; Martelli, P.; Pendollino, F.; Friedrichs, O.; Züttel, A.; Embs, J. *P. J. Phys. Chem. C* **2009**, *113*, 16834.
- (25) Remhof, A.; Łodziana, Z.; Martelli, P.; Friedrichs, O.; Züttel, A.; Skripov, A. V.; Embs, P. J.; Strässle, T. *Phys. Rev. B* **2010**, *81*, 214304.
- (26) Verdal, N.; Hartman, M. R.; Jenkins, T.; DeVries, D. J.; Rush, J. J.; Udrovic, T. *J. Phys. Chem. C* **2010**, *114*, 10027.
- (27) Blanchard, D.; Riktor, M. D.; Maronsson, J. B.; Jacobsen, H. S.; Kehres, J.; Sveinbjörnsson, D.; Bardaji, E.-G.; Léon, A.; Juranyi, F.; Wuttke, J.; Hauback, B. C.; Fichtner, M.; Vegge, T. *J. Phys. Chem. C* **2011**, *114*, 479.
- (28) Martelli, P.; Remhof, A.; Borgschulte, A.; Ackermann, R.; Strässle, T.; Embs, J. P.; Ernst, M.; Matsuo, M.; Orimo, S.-I.; Züttel, A. *J. Phys. Chem. A* **2011**, *115*, 5329.
- (29) Tomkinson, J.; Waddington, T. *C. J. Chem. Soc. Faraday* **1976**, *72*, 528.
- (30) Borgschulte, A.; Gremaud, R.; Zuttel, A.; Martelli, P.; Ramirez-Cuesta, A. J.; Refson, K.; Bardaji, E. G.; Lohstroh, W.; Fichtner, M.; Hagemann, H.; Ernst, M. *Phys. Rev. B* **2011**, *83*, 024102–024101.
- (31) Bée, M. *Quasielastic Neutron Scattering*; Adam Hilger: Bristol, UK, 1988.
- (32) Cerny, R.; Filinchuk, Y.; Hagemann, H.; Yvon, K. *Angew. Chem., Int. Ed.* **2007**, *46*, 5765.
- (33) Her, J.-H.; Stephens, P. W.; Gao, Y.; Soloveichik, G. L.; Rijssenbeek, J.; Andrus, M.; Zhao, J.-C. *Acta Crystallogr.* **2007**, *B63*, S61.
- (34) Konoplev, V. N.; Bakulina, V. M. *Bull. Acad. Sci. USSR Div. Chem. Sci. (Engl. Transl.)* **1971**, *20*, 136.
- (35) George, L.; Drozd, V.; Saxena, S. K. *J. Phys. Chem. C* **2009**, *113*, 15087.
- (36) Dai, B.; Sholl, D. S.; Johnson, J. K. *J. Phys. Chem. C* **2008**, *112*, 4391.
- (37) Voss, J.; Hummelshøj, J. S.; Łodziana, Z.; Vegge, T. *J. Phys.: Condens. Matter* **2009**, *21*, 012203.
- (38) Bil, A.; Kolb, B.; Atkinson, R.; Pettifor, D. G.; Thonhauser, T.; Kolmogorov, A. N. *Phys. Rev. B* **2011**, *83*, 224103.
- (39) Yang, J.; Zhang, X.; Zheng, J.; Songa, P.; Li, X. *Scr. Mat.* **2011**, *64*, 225.
- (40) Chlopeck, K.; Frommen, C.; Léon, A.; Zabara, O.; Fichtner, M. *J. Mater. Chem.* **2007**, *17*, 3496.
- (41) Łodziana, Z.; Van Setten, M. *J. Phys. Rev. B* **2010**, *81* (2), 024117.
- (42) Hunter, B. *IUCR Powder Diffraction Newsletter*; No. 20, 1998.
- (43) Wuttke, J. *Spheres Online Manual*; http://www.jcns.info/jcns_spheres.
- (44) <http://sinq.web.psi.ch/sinq/instr/mars.html>.
- (45) Wuttke, J. *Slaw: Neutron Scattering Histograms to Scattering Law Converter*; <http://www.messen-und-deutzen.de/slaw>.
- (46) Azuah, R. T.; Kneller, L. R.; Qiu, Y.; Tregenna-Piggott, P. L. W.; Brown, C. M.; Copley, J. R. D.; Dimeo, R. M. *J. Res. Natl. Inst. Stand. Technol.* **2009**, *114*, 341.
- (47) Bahn, S. R.; Jacobsen, K. W. *Comput. Sci. Eng.* **2002**, *4*, 56.
- (48) Hammer, B.; Hansen, L. B.; Nørskov, J. K. *Phys. Rev. B* **1999**, No. 59, 7413.
- (49) Kohn, W.; Sham, L. *J. Phys. Rev.* **1965**, *140* (4A), 1133–1138.
- (50) Vanderbilt, D. *Phys. Rev. B* **1990**, *41* (11), 7892–7895.
- (51) Perdew, J. P.; Chevary, J. A.; Vosko, S. H.; Jackson, K. A.; Pederson, M. R.; Singh, D. J.; Fiolhais, C. *Phys. Rev. B* **1992**, *46* (11), 6671.
- (52) Liu, D. C.; Nocedal, J. *Math. Program.* **1989**, *45* (3), 503–528.
- (53) Henkelman, G.; Uberuaga, B. P.; Jonsson, H. *J. Chem. Phys.* **2000**, *113* (22), 9901.
- (54) Bitzek, E.; Koskinen, P.; Gähler, F.; Moseler, M.; Gumbsch, P. *Phys. Rev. Lett.* **2006**, *97* (17), 170201.
- (55) Vineyard, G. H. *J. Phys. Chem. Solids* **1957**, *3* (1–2), 121–127.
- (56) Ericsson, A.; Kowalewski, J. *J. Mag. Reson.* **1980**, *38*, 9.
- (57) Bernassau, J. M.; Fetizon, M.; Pinheiro, J. A. *J. Phys. Chem.* **1986**, *90*, 1051.
- (58) Schoenflies, A. *Math. Ann.* **1889**, *34*, 172–203.
- (59) Chahid, A.; Alegría, A.; Colmenero, J. *Macromolecules* **1994**, *27*, 3282.
- (60) Senent, M. L.; Ruiz, R.; Villa, M.; Domínguez-Gómez, R. *J. Chem. Phys.* **2009**, *130*, 064101.
- (61) Filinchuk, Y.; Cerny, R.; Hagemann, H. *Chem. Mater.* **2009**, *21*, 925.
- (62) Shane, D. T.; Bowman, R. C.; Conradi, M. S. *J. Phys. Chem. C* **2009**, *113* (42), 5039.
- (63) Corey, R. L.; Shane, D. T.; Bowman, R. C.; Conradi, M. S. *J. Phys. Chem. C* **2008**, *112* (47), 18706.
- (64) Borgschulte, A.; Zuttel, A.; Hug, P.; Racu, A. M.; Schoenes, J. *J. Phys. Chem. A* **2008**, *112* (21), 4749.
- (65) Gremaud, R.; Łodziana, Z.; Hug, P.; Willenberg, B.; Racu, A.-M.; Schoenes, J.; Ramirez-Cuesta, A. J.; Clark, S. J.; Refson, K.; Züttel, A.; Borgschulte, A. *Phys. Rev. B* **2009**, *80*, 100301–1001–4.
- (66) Léon, A.; Wuttke, J. *J. Phys.: Condens. Matter* **2011**, *23*, 254214.
- (67) Pitt, M.; Webb, C.; Paskevicius, M.; Sheptyakov, D.; Buckley, C.; Gray, E. *J. Phys. Chem. C* **2011**, *115* (45), 22669.